Circuit-model analysis for spintronic devices with chiral molecules as spin injectors

Xu Yang,* Tom Bosma, Bart J. van Wees, and Caspar H. van der Wal
Zernike Institute for Advanced Materials, University of Groningen, NL-9747AG Groningen, The Netherlands

(Received 11 April 2019; revised manuscript received 7 June 2019; published 20 June 2019)

Recent research discovered that charge-transfer processes in chiral molecules can be spin-selective, and the effect was named chiral-induced spin selectivity (CISS). Follow-up work studied hybrid spintronic devices with conventional electronic materials and chiral (bio)molecules. However, a theoretical foundation for the CISS effect is still in development, and the spintronic signals were not evaluated quantitatively. We present a circuit-model approach that can provide quantitative evaluations. Our analysis assumes the scheme of a recent experiment that used photosystem I (PSI) as spin injectors, for which we find that the experimentally observed signals are, under any reasonable assumptions on relevant PSI timescales, too high to be fully due to the CISS effect. We also show that the CISS effect can in principle be detected using the same type of solid-state device, and by replacing silver with graphene, the signals due to spin generation can be enlarged four orders of magnitude. Our approach thus provides a generic framework for analyzing these types of experiments and advancing the understanding of the CISS effect.

DOI: 10.1103/PhysRevB.99.214428

I. INTRODUCTION

Electronic spin lies at the heart of spintronics due to its ability to convey digital information. In contrast, this quantum-mechanical concept has found few applications in chemistry and biology as the energy states associated with opposite spin orientations are often degenerate. Molecular chirality, on the other hand, is thoroughly discussed in chemistry and biology but rarely addressed in spintronics. In the past decade, the two concepts have been increasingly linked thanks to the discovery of the chiral-induced spin selectivity (CISS) effect, which describes that the electron transfer in chiral molecules is spin-dependent [1–11]. This discovery not only provides new approaches to controlling chiral molecules [12] and understanding their interactions [13], but it also opens up the possibility of small, flexible, and fully organic spintronic devices. Previously, organic materials were incorporated in spintronic devices as spin transport channels and spin-charge converters, but the conversion efficiency remained low [14–22]. Building on CISS, hybrid devices with efficient molecular spin injectors and detectors were realized [23–32]. However, a full understanding of the signals produced by these devices is still lacking, and thereby the understanding of CISS largely hindered.

We present here a circuit-model approach to quantitatively evaluating the spin signals measured from hybrid solid-state devices designed for studying the CISS effect. Similar approaches have been used for the analyses of spintronic devices with metallic and semiconducting materials [33–35]. They provided accurate descriptions of experimental results and have been extended to a wide range of device geometries. We apply here such modeling to devices with adsorbed molecular active layers instead of metal contacts. While generally applicable, we take the device reported in Ref. [26] as a case study for demonstrating our approach. In comparison to our recent analysis using electron-transmission modeling [36], the circuit-model approach is more suited for including a role for optically driven chiral molecules, and for electron transport outside the linear-response regime.

In the work of Ref. [26], cyanobacterial photosystem I (PSI) protein complexes were self-assembled on a silver-AlO_x-nickel junction, and the orientation of PSI (*up* or *down*) was controlled by mutations and linker molecules. Figure 1 shows a device with PSI in the *up* orientation. Here, P700, the reaction center of PSI, was located adjacent to the silver layer. In P700, charge separation took place upon the illumination of a 660-nm laser during the experiments. It was described that the excited electron got transferred to the Fe_4S_4 clusters at the other end of PSI, and the hole left behind in P700 was refilled by an electron from silver. This process causes a net *upward* electron transfer from silver to PSI, which, before relaxation, results in a steady-state increase of the silver surface potential, as was observed using a Kelvin probe [26]. In contrast, a device with PSI in the *down* orientation gave a decrease of silver surface potential upon light illumination, indicating a net *downward* electron transfer from PSI into silver. Both devices were then placed under laser illumination in the presence of an out-of-plane magnetic field, which was used to set the magnetization of nickel in either the *up* or *down* direction. The charge voltage between silver and the nickel layer was monitored. The absolute value of this voltage was found to be always lower when the electron transfer direction and the magnetic field direction were parallel (both *up* or both *down*), and higher when they were antiparallel (one *up* and one *down*). This magnetic field dependence suggested that the electron transfer process in PSI was spin-selective, and the preferred spin orientation was parallel to the electron momentum. As PSI is one of nature's two major light-harvesting centers, this intriguing result indicated that electron spins may also play a role in photosynthesis.

*xu.yang@rug.nl

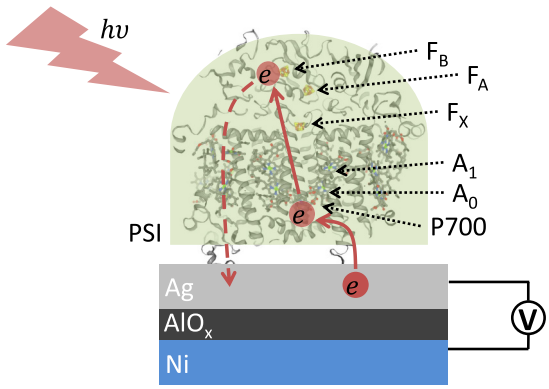

FIG. 1. Electron transfer chain of PSI and the geometry of the solid-state device used in Ref. [26]. The device was a stack of 150 nm of nickel, 0.5 nm of AlO_x, and 50 nm of silver. PSI was immobilized on top of the silver layer, and the voltage difference between the silver and the nickel was measured. PSI is represented by the green area on which the structure of a part that contains the PSI electron transfer chain is overlaid. The structure highlights key cofactors such as Fe_4S_4 clusters (F_B, F_A, and F_X), primary electron acceptors (A_1 and A_0), the reaction center (P700), and the chiral (helical) structural surroundings. Here PSI is in the *up* orientation, with P700 close to silver, and the Fe_4S_4 clusters at the far end. Red labelings mark the light-induced electron transfer process, including the photon ($h\nu$) and the electron (e), the photoexcitation pathway (solid arrows), and the unknown relaxation pathway (dashed arrow). The protein structure is taken from the RCSB Protein Data Bank (PDB ID 1JB0) [37].

However, an important question to address while considering this conclusion is as follows: How much of the observed magnetic-field-dependent signal was from CISS? To answer this question, we need to understand the origin of the measured steady-state magnetic-field-dependent voltage. Upon photoexcitation, charge carriers were transferred from silver to PSI. These carriers must relax back to silver via pathways inside PSI because there was no top electrode providing alternative pathways. Both the excitation and relaxation pathways might exhibit spin selectivity. Qualitatively, as long as the CISS effects in the two pathways do not cancel each other, a net spin injection into silver can be generated. This spin injection then competes with the spin relaxation process in silver, and results in a steady-state spin accumulation that can indeed be detected as a charge voltage between silver and the nickel layer [38].

II. CIRCUIT-MODEL ANALYSIS

To quantitatively evaluate this voltage signal, we adopt a two-current circuit model where spin transport is described by two parallel channels (spin-up and spin-down channels) [39,40]. The two channels are connected via a spin-flip resistance $R_{\rm sf}$, which characterizes the spin relaxation process in a nonmagnetic material. A derivation of $R_{\rm sf}$ and a more detailed introduction of the two-current model concept can be found in Appendix A. For a thin-film nonmagnetic material, we find

$$R_{\rm sf} = 2\frac{\lambda_{\rm sf}^2}{dA_{\rm rel}\,\sigma} \tag{1}$$

(assuming $d < \lambda_{\rm sf}$ and $A_{\rm rel} \gg \lambda_{\rm sf}^2$), where $\lambda_{\rm sf}$ is the spin-relaxation length of the material, σ is the conductivity of the material, d is the thickness of the film, and $A_{\rm rel}$ is the relevant area of the film where spin injection occurs. Notably, $R_{\rm sf}$ is entirely determined by the properties of the material and the geometry of the device.

The role of PSI in the device can be characterized by two features. First, due to the lack of a top electrode, there was (as a steady-state average) no net charge current flowing through PSI. Secondly, facilitated by CISS, PSI gave a net spin injection into silver. These two features resemble a pure spin-current source. Therefore, we model PSI as a pure spin-current source between the fully polarized spin-up (red) and spin-down (blue) channels, as shown in Fig. 2(a). Upon photoexcitation, PSI sources an internal spin current $I_{\rm PSI}$. The pathway with spin-flip resistance $R_{\text{sf-PSI}}$ accounts for the spin relaxation inside PSI. At the PSI-silver interface, the two channels encounter possibly spin-dependent contact resistances $R_{\text{cPSI}\uparrow}$ and $R_{\text{cPSI}\downarrow}$. The net spin current injected from PSI into silver is $I_s = \eta I_{\rm PSI}$ $(-1 \leqslant \eta \leqslant 1)$, with η being the fraction of the photoinduced spin current that actually contributes to the spin accumulation in silver. Generically, we regard PSI as a black box: a two-terminal unit that drives a spin current I_s, as shown in Fig. 2(b). This will later be linked and compared to known timescales for charge-transfer processes inside PSI.

A circuit model for the entire device is shown in Fig. 3. $R_{\rm Ag}$ is the spin-independent resistance (in the out-of-plane direction) of the silver layer. Inside the silver layer, the spins can relax, as represented by a spin-flip pathway with resistance $R_{\text{sf-Ag}}$. $R_{\rm cAg}$ is the contact resistance between silver and the voltage meter. In principle, these contacts could provide an extra pathway for electron spins to relax, but in reality these contacts are located millimeters away from where spins are injected. This distance is much larger than the spin-relaxation length in silver (about 150 nm at room temperature) [41]. Therefore, the spin relaxation through these contacts is negligible and we can assume $R_{\rm cAg} \to \infty$.

Underneath the silver layer is the AlO_x tunnel barrier and the ferromagnetic nickel layer. In these layers, electrons experience spin-dependent resistances: the tunnel resistance $R_{\text{tun}\uparrow(\downarrow)}$ and the contact resistance $R_{\text{cNi}\uparrow(\downarrow)}$ (which includes the out-of-plane resistance of the nickel layer). Note that here the subscript $\uparrow$ $(\downarrow)$ refers to the corresponding spin-current channel, not to be confused with the magnetization direction of nickel, which determines the values of $R_{\text{tun}\uparrow(\downarrow)}$ and $R_{\text{cNi}\uparrow(\downarrow)}$. These resistances can be combined using shorter notations $R_\uparrow = R_{\text{tun}\uparrow} + R_{\text{cNi}\uparrow}$ and $R_\downarrow = R_{\text{tun}\downarrow} + R_{\text{cNi}\downarrow}$. An interchange of the $R_\uparrow$ and $R_\downarrow$ values thus accounts for the reversal of the magnetization direction of nickel.

The magnetization direction of nickel can be described as being parallel (p) or antiparallel (ap) to the spin-up channel. For each case, the reading of the voltage meter $V_{\rm meas}$ is

$$V_{\rm meas}^{\rm (p)} = \frac{1}{2} I_s (R_\uparrow - R_\downarrow) \frac{R_{\text{sf-Ag}}}{R_\uparrow + R_\downarrow + R_{\text{sf-Ag}}}, \tag{2a}$$

$$V_{\rm meas}^{\rm (ap)} = \frac{1}{2} I_s (R_\downarrow - R_\uparrow) \frac{R_{\text{sf-Ag}}}{R_\uparrow + R_\downarrow + R_{\text{sf-Ag}}}. \tag{2b}$$

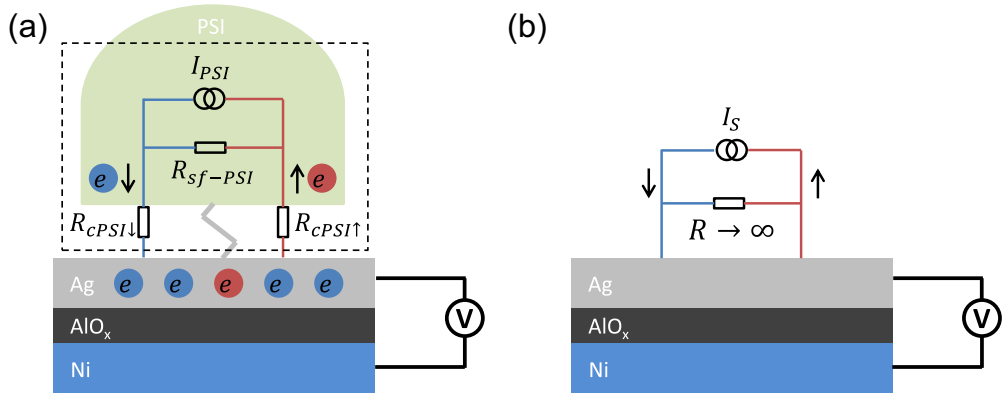

FIG. 2. PSI modeled as a spin-current source. (a) PSI compared to a pure spin-current source with a spin relaxation pathway. It creates spin accumulation in the silver layer upon light illumination. Spin-up electrons (red) are transferred from silver to PSI, while spin-down electrons (blue) are transferred back to silver. No charge current flows through PSI, but a spin-down accumulation is created in silver. (b) The model of panel (a), reduced to its net spin-injection effect. The contribution from each component in the dashed box in (a) cannot be clearly distinguished, therefore we treat them together as an ideal spin-current source I_s with a parallel resistance R. Since the total impedance in PSI is much larger than that of silver, we consider $R \to \infty$. The net effect of this reduced model is to inject a spin current I_s into the silver layer. Here we show the drawing for one PSI unit, but the spin currents ($I_{\rm PSI}$, I_s) concern the values for the entire PSI ensemble on the device.

The change in the measured voltage upon the reversal of the nickel magnetization is therefore

$$\begin{aligned} V_{\rm diff} &= V_{\rm meas}^{\rm (ap)} - V_{\rm meas}^{\rm (p)} \\ &= I_s(R_\downarrow - R_\uparrow)\frac{R_{\rm sf\text{-}Ag}}{R_\uparrow + R_\downarrow + R_{\rm sf\text{-}Ag}} \\ &= I_s R_{\rm eff}, \end{aligned} \tag{3}$$

where $R_{\rm eff} = V_{\rm diff}/I_s$ is an effective spin-valve resistance.

For the envisioned spintronic behavior in Ref. [26], this model captures all relevant aspects for spintronic signals in the linear transport regime, without making assumptions that restrict its validity. It is thus suited for describing the observed spin signals in a quantitative manner when the values of the circuit parameters are available. For the device described in Ref. [26], we derive (see Appendix B)

$$R_{\rm eff} \approx 15\ {\rm m}\Omega. \tag{4}$$

Note that $R_{\rm eff}$ is fully determined by the properties of the Ag-AlO_x-Ni multilayer, and deriving its value does not use any estimates or assumptions concerning PSI. Furthermore, by carefully choosing material parameters, the estimate of $R_{\rm eff}$ is of great accuracy. This is also discussed in Appendix B.

This result for $R_{\rm eff}$ directly yields values for the injected spin current that was flowing in the experiment of Ref. [26]. For the *up* orientation of PSI, the measured voltage difference $V_{\rm diff}$ was about 50 nV. Thus, the net spin current injected into silver must have been $I_s = V_{\rm diff}/R_{\rm eff} \approx 3\ \mu$A. For the opposite PSI orientation, the measured $V_{\rm diff}$ was about 10 nV, and accordingly $I_s \approx 0.6\ \mu$A.

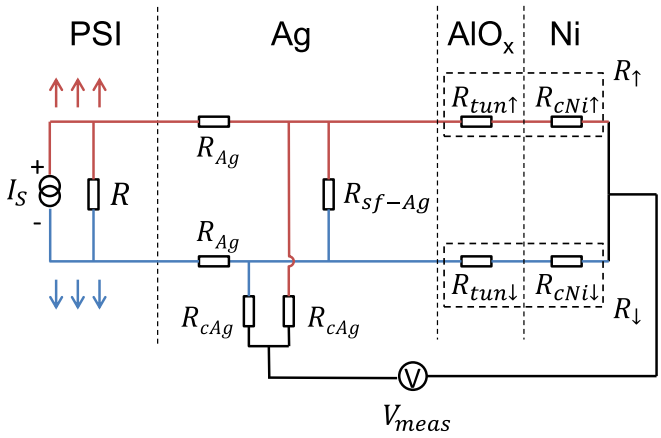

FIG. 3. Two-current circuit model for the spintronic device of Ref. [26] (symbols introduced in the main text). Different parts of the device are separated by dashed lines. Spin-up and spin-down current channels are distinguished by color. PSI is represented by a pure spin-current source as introduced in Fig. 2(b). The spin relaxation in silver is modeled as a pathway with spin-flip resistance $R_{\rm sf\text{-}Ag}$ connecting the two spin-current channels.

III. DISCUSSIONS

Next, we turn these spin-current values into values for the timescale τ that must then hold for the charge excitation-relaxation process for illuminated PSI. Here τ can be understood as the time interval between two consecutive photoexcitation processes from the same PSI unit. By assuming that the intensity of the illumination is strong enough to drive all the PSI units in continuous excitation-relaxation cycles (saturated), we can write $i = -e/\tau$, where e is the elementary charge and i is the photoinduced charge current in a PSI unit. The sum of all contributions i (sum over all PSI units) should then be high enough to provide the above I_s values. To check this, we will assume the highest number for PSI units that can contribute, and that they all maximally contribute. Therefore, we first assume that over the relevant area of the device, the PSI units form a densely packed, fully oriented monolayer, and that all PSI units function identically. Secondly, we assume that photoinduced spin current from each PSI unit is fully injected into the silver layer, i.e., $\eta = 1$. Further, we assume that the polarization of the CISS effect in PSI is 50%, on par with the reported CISS polarization in

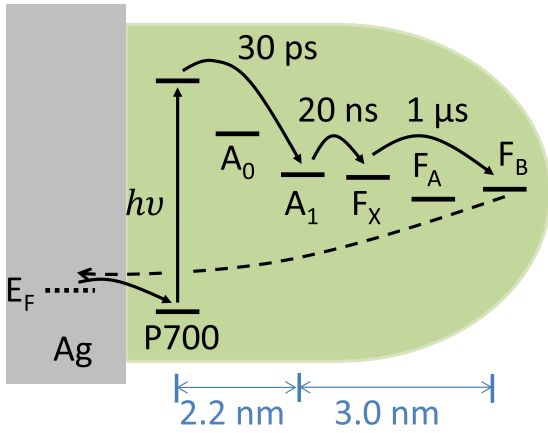

FIG. 4. Electron transfer process and corresponding timescales in PSI, here depicted in a manner where the vertical placements of states reflect their energy levels. Here the PSI unit is in the *up* orientation. The excitation process is labeled by the black arrows with corresponding timescales marked. However, the relaxation process is unknown (dashed arrow). The blue scale shows the spatial distance between different parts of the electron transfer chain.

other chiral systems [3,8,26]. For these assumptions, we find (details are in Appendix C) that for the *up* orientation of PSI, τ should not be larger than 100 ps. For the *down* orientation, this limit is $\tau \leqslant 500$ ps. Note that the boundaries here correspond to the most ideal scenario, and in practice the required τ values could be much smaller than these boundaries.

We now compare these requirements for τ with the well-studied timescales of the electron transfer process in PSI. During photosynthesis, the photoinduced charge separation in PSI takes place at the primary donor P700. Electrons are then transferred through a series of accepters along the electron transfer chain: A_0, A_1, and the Fe_4S_4 clusters F_X, F_A, and F_B (see Fig. 4) [37,42,43]. The initial electron transfer from P700 to A_1 is ultrafast (∼30 ps), and further transfer to F_X happens in 20–200 ns. Then, the electron transfer from F_X through F_A to F_B typically takes 500 ns to 1 μs [43].

The requirements for τ values that we found are—regardless of the PSI orientation—only compatible with the initial ultrafast electron transfer from P700 to A_1. The subsequent steps are at least two orders of magnitude too slow. Thus, concluding that the observed signals fully result from the CISS effect requires the existence of an ultrafast relaxation process where electrons immediately return to P700 after their initial transfer from P700 to A_1. This process does not exist in nature, because it would stop the transmembrane electron transfer in photosynthesis. We should nevertheless consider whether it can occur in the device, since PSI is located there in a very different environment.

In the solid-state environment, faster relaxation than in nature could be due to, for instance, the use of linker molecules, the mutations of PSI, or the presence of silver (thanks to its high density of states). The linker molecules are unlikely to be the reason, because their size is significantly smaller than PSI, and the electron transfer chain is positioned deeply in the center of PSI (Fig. 4). Moreover, it was stated in Ref. [26] that the observed signals do not depend on the linker molecules.

The mutations and the metal substrate, on the other hand, could indeed affect the electron transfer. To assess the effects, we can draw direct comparisons between Refs. [26] and [44]. In both works, the same mutations of PSI were performed in order to covalently bind PSI to metal substrates (Ag and Au, respectively). Reference [44] found, for the bound PSI, the fastest excitation-relaxation cycle of around 15 ns. For Ref. [26], the value should be on the same order of magnitude due to the large similarities between the two experiments. However, this value is still two orders of magnitude slower than the most ideal scenario that we have assumed. Therefore, the CISS-related spin signals in Ref. [26] were at least two orders of magnitude lower than the measured value. In fact, if we consider a realistic situation in which PSI units do not form a fully oriented and densely packed layer on silver and $|\eta| < 1$, the actual CISS signals should be even smaller.

Although other mechanisms may still be at play [45,46], they are not able to make up for the orders of magnitude of deviation. We thus conclude that the observed signals in Ref. [26] cannot be fully due to the light-induced spin injection from PSI, unless the very similar PSI conditions in Refs. [26] and [44] could lead to orders of magnitude of difference in PSI charge-transfer timescales. This suggests that the magnetic-field dependence of the signals in Ref. [26] may predominantly originate from other effects. Some possible sources are discussed in Appendix D.

Nevertheless, our analysis shows that an experimental approach as in Ref. [26] is in principle suited for confirming spin signals with CISS origin. It also provides insight into how one can optimize this type of experiment toward a system that would yield CISS spin signals with a higher magnitude. The most direct improvement can be obtained via a system that has higher values for R_{sf} and R_{eff} in Eqs. (1)–(4). A good example to consider is to use graphene as a replacement for the silver layer. This should boost the spin signals by four orders of magnitude, since it would increase the value of R_{eff} from ∼15 mΩ to a value of ∼0.5 kΩ (see Appendix B for details).

IV. CONCLUSION

In summary, we introduced a two-current circuit-model approach to quantitatively assess spintronic signals in hybrid devices that combine conventional electronic materials with (bio)organic molecules that are spin-active due to the CISS effect. As an example, we applied it to a case in which the active layer has electrical contact only on one side, and we showed how the quantitative analysis can link the observed spin signals to charge excitation and relaxation times in the molecules. Our analysis showed that such devices can readily give spintronic signals that are strong enough for detection with current technologies. However, it also revealed that in the experiment of our case study (Ref. [26]), the observed signals must have had strong contributions from other effects. Future experimental work should aim at separating other signals from signals given by CISS, and our circuit-model approach assists in designing these experiments. We also recommend using devices with nonlocal geometries in order to separate charge and spin signals [36,38]. In these geometries, the spin signals can also be quantitatively assessed using our circuit-model approach.

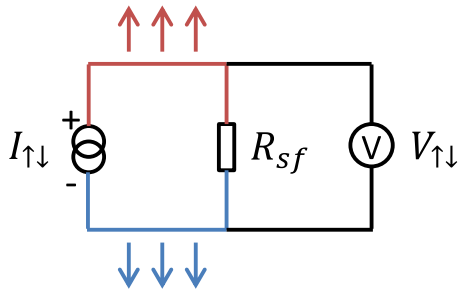

FIG. 5. A circuit model considering the spin injection in a nonmagnetic conducting material. Spin-up and spin-down components are separated into red and blue channels. A pure spin current $I_{\uparrow\downarrow}$ is sourced between the two channels. Spin relaxation is modeled as a spin-flip resistance $R_{\rm sf}$. The spin accumulation is measured as the signal $V_{\uparrow\downarrow}$ from a voltage meter that has fully spin-selective contacts.

ACKNOWLEDGMENTS

The authors acknowledge the financial support from the Zernike Institute for Advanced Materials (ZIAM), and the Spinoza prize awarded to B.J.v.W. by the Nederlandse Organisatie voor Wetenschappelijk Onderzoek (NWO). We thank A. Herrmann and P. Gordiichuk for stimulating discussions.

APPENDIX A: TWO-CURRENT MODEL AND DERIVATION OF $R_{\rm sf}$

In this Appendix, we use a simple example to introduce the concept of two-current circuit models [39,40] and to illustrate what can be experimentally detected. Along the way, we derive $R_{\rm sf}$ [Eq. (1)].

For describing spintronic signals, we use modeling where spin transport in conductors is described as two parallel channels each allowing only one type of spin (spin-up and spin-down channels, colored in red and blue, respectively, in Fig. 5) [39,40]. This allows us to separate the total electrical current I into spin-up and spin-down components: $I = I_\uparrow + I_\downarrow$. The difference between the two components is referred to as a spin current $I_{\uparrow\downarrow}$, with $I_{\uparrow\downarrow} = I_\uparrow - I_\downarrow$. A spin current injected into a nonmagnetic material will result in a spin accumulation (chemical potential difference between the spin-up and spin-down channels) $\mu_{\uparrow\downarrow} = \mu_\uparrow - \mu_\downarrow$. Within the material, spin accumulation decays exponentially over time due to spin relaxation mechanisms [47]. As an introduction to this type of modeling, we first show a simple case with a pure spin current in a nonmagnetic material, as shown in Fig. 5. A pure spin current means that the net charge current $I = I_\uparrow + I_\downarrow = 0$. The spin relaxation is modeled as a pathway connecting the two channels, with a spin-flip resistance $R_{\rm sf}$. The voltage difference between the two channels, as measured with fully spin-selective contacts, is therefore $V_{\uparrow\downarrow} = I_{\uparrow\downarrow} R_{\rm sf}$.

Within the nonmagnetic material, the steady-state spin accumulation is a balance between the spin injection due to $I_{\uparrow\downarrow}$ and the spin relaxation in the material. This is described as

$$0 = \frac{d\mu_{\uparrow\downarrow}}{dt} = -\frac{\mu_{\uparrow\downarrow}}{\tau_{\rm sf}} + 2\frac{I_{\uparrow\downarrow}}{e}\frac{1}{\nu_{\rm 3D} V_{\rm rel}}, \tag{A1}$$

where $\tau_{\rm sf}$ is the spin-relaxation time in the material, $\nu_{\rm 3D}$ is the three-dimensional (3D) density of states (units of $\mathrm{eV}^{-1}\,\mathrm{m}^{-3}$), and $V_{\rm rel}$ is the relevant volume for the spin injection-relaxation balance in the material. The factor 2 arises from the fact that when one electron is transferred from the spin-down channel to the spin-up channel, the difference between the spin-up and spin-down population increases by 2. The steady-state solution for the measured voltage is

$$V_{\uparrow\downarrow} = \frac{\mu_{\uparrow\downarrow}}{e} = I_{\uparrow\downarrow}\frac{1}{V_{\rm rel}}\frac{1}{\nu_{\rm 3D}}\frac{2\tau_{\rm sf}}{e^2}. \tag{A2}$$

For further analysis, we also consider the role of the spin relaxation length of the material, $\lambda_{\rm sf} = \sqrt{D\tau_{\rm sf}}$, where D is the diffusion coefficient for electrons in the material. The Einstein relation gives $\sigma = e^2\nu_{\rm 3D}D$, where σ is the conductivity of the material [38]. Consequently, Eq. (A2) becomes

$$V_{\uparrow\downarrow} = 2I_{\uparrow\downarrow}\frac{\lambda_{\rm sf}^2}{V_{\rm rel}\,\sigma}, \tag{A3}$$

and therefore

$$R_{\rm sf} = \frac{V_{\uparrow\downarrow}}{I_{\uparrow\downarrow}} = 2\frac{\lambda_{\rm sf}^2}{V_{\rm rel}\,\sigma}. \tag{A4}$$

We can see that the spin-flip resistance is completely determined by the properties of the material and the relevant volume concerned for each specific device.

Now we determine the relevant volume $V_{\rm rel}$ for a particular device geometry: a thin layer of a nonmagnetic conducting material. The spin accumulation spreads out in a volume that is limited by either the spin relaxation length $\lambda_{\rm sf}$ or the boundaries of the device, whichever is smaller. For the thin layer, we assume that the spin current is homogeneously injected from its top surface over a limited area, which is referred to as the relevant area $A_{\rm rel}$. Spin accumulation then occurs in the thin layer within the area $A_{\rm rel}$, as well as directly outside the boundaries of $A_{\rm rel}$, up to a distance of $\sim\lambda_{\rm sf}$. However, we consider here the situation in which $A_{\rm rel} \gg \lambda_{\rm sf}^2$, and we can therefore neglect the spin accumulation outside $A_{\rm rel}$. In the perpendicular direction, we consider the case in which the thickness of the layer $d < \lambda_{\rm sf}$, which means that the spin-transport length is limited by the thickness of the layer rather than the spin relaxation length of the material. As a consequence, we have $V_{\rm rel} = dA_{\rm rel}$. Substituting this into Eq. (A4) gives

$$R_{\rm sf} = 2\frac{\lambda_{\rm sf}^2}{dA_{\rm rel}\,\sigma}. \tag{A5}$$

When the thin layer (three-dimensional) is replaced by a truly two-dimensional material, such as graphene, the thickness of the material can no longer be defined. The material then has a two-dimensional density of states $\nu_{\rm 2D}$ (units of $\mathrm{eV}^{-1}\,\mathrm{m}^{-2}$), and one should use the Einstein relation for the 2D conductivity $\sigma_{\rm 2D} = e^2\nu_{\rm 2D}D$. When assuming again $A_{\rm rel} \gg \lambda_{\rm sf}^2$, the spin-flip resistance for a 2D system is given as

$$R_{\text{sf-2D}} = 2\,\frac{\lambda_{\rm sf}^2}{A_{\rm rel}\,\sigma_{\rm 2D}}. \tag{A6}$$

APPENDIX B: ESTIMATE FOR THE VALUE OF R_{eff}

In this Appendix, we estimate a value for the effective spin-valve resistance R_{eff}. We first focus on a value for the experimental work of Ref. [26], and then on a similar system that has the silver layer replaced by graphene.

The tunneling resistance between silver and nickel was measured to be about 1 kΩ in Ref. [23], which used a device identical to that in Ref. [26]. The change of this resistance under magnetization reversal, as characterized by its tunneling magnetoresistance [TMR $= (R_\downarrow - R_\uparrow)/R_\uparrow$], depends on the spin polarization of nickel P_{Ni}, and it does not depend on the magnetization axis [48–50]. It follows that TMR $= 2P_{\text{Ni}}/(1 - P_{\text{Ni}})$, and takes a value of TMR $\approx 100\%$ for the $P_{\text{Ni}} \approx 33\%$ value used in Ref. [26]. The actual TMR value may be lower than 100% because of temperature and bias voltage, but it should be on the same order of magnitude [50,51]. Moreover, taking the upper limit of TMR is consistent with us deriving the lower limit of I_s and the upper limit of τ. Therefore, we may assume $R_\downarrow = 1$ kΩ and $R_\uparrow = 0.5$ kΩ. While this is an estimate, the value must be of the correct order of magnitude. Furthermore, later analysis will show that it is the spin-flip resistance of silver that governs the magnitude of the effective resistance R_{eff}.

To determine the spin-flip resistance of silver, we use the previously derived Eq. (A5). For the device we discuss, the thickness of the silver layer $d = 50$ nm, and the area of the junction $A_{\text{rel}} = 1\ \mu\text{m} \times 1\ \mu\text{m}$. For spin relaxation parameters, we take reported values for a mesoscopic silver strip at room temperature, $\lambda_{\text{sf-Ag}} \approx 150$ nm, and $\rho_{\text{Ag}} = 1/\sigma_{\text{Ag}} \approx 50$ nΩ m [41]. We point out that these parameters are not only affected by the material choice, but also by factors such as device geometry, fabrication techniques, and temperature [52]. The values we chose were reported for a device that had geometries very close to that used in Ref. [26], was fabricated with the same technique, and was measured at the same temperature. With these, we get the spin-flip resistance in our model, $R_{\text{sf-Ag}} = 45$ mΩ.

Substituting $R_{\text{sf-Ag}}$, together with the assumed $R_\uparrow, R_\downarrow$ values in Eq. (3), gives an effective resistance

$$R_{\text{eff}} \approx 15\ \text{m}\Omega. \tag{B1}$$

Note that R_{eff} is fully determined by the properties of the Ag-AlO_x-Ni multilayer device, and estimating its value did not use any estimates or assumptions concerning PSI.

For the scenario in which the silver layer is replaced by a graphene layer, we apply a similar analysis while using Eq. (A6) instead of Eq. (A5). For graphene, typical material parameters are a square resistance of the order of 1 kΩ [53,54], and a spin relaxation length of $\lambda_{\text{sf}} \approx 10\ \mu$m [54,55]. This gives $R_{\text{sf-2D}} \approx 1$ MΩ and $R_{\text{eff}} \approx 0.5$ kΩ for a device that is for other aspects identical to the device of Ref. [26].

APPENDIX C: ANALYSIS OF COMPATIBLE PSI EXCITATION AND RELAXATION TIMES

In the main text, we derived the I_s values without using any information about PSI. Here we analyze what the values mean in terms of photoexcitation and relaxation times of individual PSI units. We first assume that I_s is fully induced by the spin-selective electron transfer during photoexcitation and relaxation cycles in PSI. Then we examine the validity of this assumption by deriving (from I_s) the values of photoexcitation and relaxation times of individual PSI units. In the following discussion, a few more assumptions are made. We carefully assume scenarios that consistently lead to the upper boundary of the photoexcitation-relaxation times. In the main text, we showed that even this upper boundary is still too low to be realistic.

We write I_s as a sum of the contributions from individual PSI units,

$$I_s = \sum_{n=1}^{N} i_{s,n}, \tag{C1}$$

where i_s is the spin current injected from each PSI unit into silver, the index n runs over all individual PSI units, and N is the number of PSI units within the relevant area (area of the junction) A_{rel}. We assume that all PSI units are oriented in the same direction, so that each of them contributes equally to the total current I_s. Therefore, we have $i_{s,n} \equiv i_s$, hence

$$I_s = i_s N = i_s \rho A_{\text{rel}}, \tag{C2}$$

where ρ is the number density, or coverage, of PSI. To estimate the coverage, we need to take into consideration the size of PSI units. Isolated cyanobacterial PSI systems usually appear in trimers with typical diameters of around 30 nm. This means three PSI units reside in an area of about 700 nm^2, or for convenience, approximately a coverage of $\rho = 0.004\ \text{nm}^{-2}$. Note that this is the highest possible coverage for a monolayer of PSI, since it corresponds to the entire silver surface being covered with a uniform, densely packed PSI layer. We assume this maximum coverage for the entire junction area. We further assume that the total injected spin current I_s is equally contributed by all the PSI units. This gives us an estimate of the lower boundary of i_s, the spin-current injection per PSI unit. For the *up* orientation of PSI, we have $i_s \geqslant 750$ pA. For the *down* orientation, this lower limit is 150 pA.

Next, we analyze the magnitude of the charge current needed to produce this spin current via the CISS effect. In our model, each PSI unit injects a spin current i_s into silver, which is a fraction of the total spin current i_{PSI} inside PSI. We have $i_s = \eta i_{\text{PSI}}$, with $-1 \leqslant \eta \leqslant 1$ being the fraction parameter. The value of η depends on the spin-relaxation process inside PSI. To obtain a lower estimate of i_{PSI}, we assume $\eta = 1$ (all the photoinduced spin current in PSI can be injected to the silver layer), hence $i_{\text{PSI}} = i_s$. This spin current, i_{PSI}, is again a fraction of the charge current i induced by the continuous electron transfer during photoexcitation and relaxation cycles in a PSI unit. The conversion from a charge current into a spin current is due to the CISS effect, and its efficiency is characterized by its polarization $P_{\text{PSI}} = i_{\text{PSI}}/i$. The CISS polarization of other chiral systems is reported to be about 50% [3,8,26], so here we adopt the same value. Taking the above into account, we can derive the lower boundary of the charge current driven by photoexcitation and relaxation processes in a PSI unit: $i \geqslant 1.5$ nA for the *up* orientation, and 300 pA for the *down* orientation.

Finally, we translate this current into a value for the excitation-relaxation time τ. Here, τ can be understood as the turnover time, or the time interval between two consecutive photoexcitation processes from the same PSI unit. By assuming the intensity of the illumination is strong enough to drive all the PSI units in continuous excitation-relaxation cycles (saturated), we can write $i = -e/\tau$. A lower boundary of i corresponds to an upper boundary of τ. For the *up* orientation of PSI, $i \geqslant 1.5$ nA corresponds to $\tau \leqslant 100$ ps. For the *down* orientation, the limit is $\tau \leqslant 500$ ps.

APPENDIX D: POSSIBLE ORIGINS OF MAGNETIC-FIELD-DEPENDENT SIGNALS IN HYBRID CISS DEVICES

There are other effects that can give rise to the magnetic-field-dependent signals in devices as used in Ref. [26]. One of these effects is the photoresponse of silver. Any modification of the silver surface can change its work function. A work function as low as 1.8 eV was reported for modified silver surfaces [56,57]. It is therefore possible that the adsorbed PSI units and binder molecules modified the silver surface in a way that photoemission was allowed at the photon energies used in the experiment. This photoemission can be spin-polarized due to the spin-orbit effect in silver and possible spin-dependent scattering at the surface [58]. Alternatively, the signals could also arise from a pure charge effect. Even without photoemission, the change of silver work function can lead to a voltage signal in the Ni-AlO_x-Ag capacitor. This voltage signal may depend on illumination and magnetic field, because the adsorbed PSI (which modifies the silver surface and thus the voltage signal) is highly photosensitive and contains large iron clusters that may respond to magnetic field. In such a scenario (where spin transport does not play a role), the orientation of PSI can only affect the magnitude but not the sign of the magnetic-field dependence. In fact, this is indeed the case if one considers the full signals reported in Figs. 2(a)(ii) and 2(b)(ii) of Ref. [26] instead of only their absolute values. In both figures, the measured signals can be separated into two parts: a nonzero background and a magnetic-field-dependent component that shows a step upon magnetic-field reversal. Figure 2(b)(ii) differs from Fig. 2(a)(ii) by having an opposite sign for the background and a smaller step size upon magnetic-field reversal. The directions of the steps (i.e., the signs of the magnetic-field dependence) in both figures are the same: Both signals shift tens of nanovolts to less positive (more negative) values when reversing the magnetic field from the *down* to *up* direction. The opposite signs for the background can be explained by the opposite orientations of PSI (just as how the PSI orientation affected the silver surface potential measured with a Kelvin probe), whereas the change of step size may be given by the change of position of the iron clusters with respect to the silver surface.

[1] K. Ray, S. P. Ananthavel, D. H. Waldeck, and R. Naaman, Asymmetric scattering of polarized electrons by organized organic films of chiral molecules, Science **283**, 814 (1999).

[2] S. Yeganeh, M. A. Ratner, E. Medina, and V. Mujica, Chiral electron transport: scattering through helical potentials, J. Chem. Phys. **131**, 014707 (2009).

[3] B. Göhler, V. Hamelbeck, T. Z. Markus, M. Kettner, G. F. Hanne, Z. Vager, R. Naaman, and H. Zacharias, Spin selectivity in electron transmission through self-assembled monolayers of double-stranded dna, Science **331**, 894 (2011).

[4] Z. Xie, T. Z. Markus, S. R. Cohen, Z. Vager, R. Gutierrez, and R. Naaman, Spin specific electron conduction through dna oligomers, Nano Lett. **11**, 4652 (2011).

[5] A.-M. Guo and Q.-F. Sun, Spin-Selective Transport of Electrons in DNA Double Helix, Phys. Rev. Lett. **108**, 218102 (2012).

[6] R. Gutierrez, E. Díaz, R. Naaman, and G. Cuniberti, Spin-selective transport through helical molecular systems, Phys. Rev. B **85**, 081404(R) (2012).

[7] E. Medina, L. A. González-Arraga, D. Finkelstein-Shapiro, B. Berche, and V. Mujica, Continuum model for chiral induced spin selectivity in helical molecules, J. Chem. Phys. **142**, 194308 (2015).

[8] K. Michaeli, N. Kantor-Uriel, R. Naaman, and D. H. Waldeck, The electron's spin and molecular chirality—how are they related and how do they affect life processes? Chem. Soc. Rev. **45**, 6478 (2016).

[9] S. Matityahu, Y. Utsumi, A. Aharony, O. Entin-Wohlman, and C. A. Balseiro, Spin-dependent transport through a chiral molecule in the presence of spin-orbit interaction and nonunitary effects, Phys. Rev. B **93**, 075407 (2016).

[10] R. Naaman and D. H. Waldeck, Chiral-induced spin selectivity effect, J. Phys. Chem. Lett. **3**, 2178 (2012).

[11] R. Naaman and D. H. Waldeck, Spintronics and chirality: Spin selectivity in electron transport through chiral molecules, Annu. Rev. Phys. Chem. **66**, 263 (2015).

[12] K. Banerjee-Ghosh, O. B. Dor, F. Tassinari, E. Capua, S. Yochelis, A. Capua, S.-H. Yang, S. S. P. Parkin, S. Sarkar, L. Kronik *et al.*, Separation of enantiomers by their enantiospecific interaction with achiral magnetic substrates, Science **360**, 1331 (2018).

[13] R. Naaman, Y. Paltiel, and D. H. Waldeck, Chirality and spin: A different perspective on enantioselective interactions, CHIMIA Int. J. Chem. **72**, 394 (2018).

[14] W. J. M. Naber, S. Faez, and W. G. van der Wiel, Organic spintronics, J. Phys. D **40**, R205 (2007).

[15] V. A. Dediu, L. E. Hueso, I. Bergenti, and C. Taliani, Spin routes in organic semiconductors, Nat. Mater. **8**, 707 (2009).

[16] D. Sun, E. Ehrenfreund, and Z. V. Vardeny, The first decade of organic spintronics research, Chem. Commun. **50**, 1781 (2014).

[17] V. Dediu, M. Murgia, F. C. Matacotta, C. Taliani, and S. Barbanera, Room temperature spin polarized injection in organic semiconductor, Solid State Commun. **122**, 181 (2002).

[18] Z. H. Xiong, D. Wu, Z. V. Vardeny, and J. Shi, Giant magnetoresistance in organic spin-valves, Nature (London) **427**, 821 (2004).

[19] L. Fang, K. D. Bozdag, C.-Y. Chen, P. A. Truitt, A. J. Epstein, and E. Johnston-Halperin, Electrical Spin Injection from an

Organic-Based Ferrimagnet in a Hybrid Organic-Inorganic Heterostructure, Phys. Rev. Lett. **106**, 156602 (2011).

[20] K. Ando, S. Watanabe, S. Mooser, E. Saitoh, and H. Sirringhaus, Solution-processed organic spin-charge converter, Nat. Mater. **12**, 622 (2013).

[21] D. Sun, K. J. van Schooten, M. Kavand, H. Malissa, C. Zhang, M. Groesbeck, C. Boehme, and Z. V. Vardeny, Inverse spin hall effect from pulsed spin current in organic semiconductors with tunable spin-orbit coupling, Nat. Mater. **15**, 863 (2016).

[22] H. Liu, C. Zhang, H. Malissa, M. Groesbeck, M. Kavand, R. McLaughlin, S. Jamali, J. Hao, D. Sun, R. A. Davidson *et al.*, Organic-based magnon spintronics, Nat. Mater. **17**, 308 (2018).

[23] K. S. Kumar, N. Kantor-Uriel, S. P. Mathew, R. Guliamov, and R. Naaman, A device for measuring spin selectivity in electron transfer, Phys. Chem. Chem. Phys. **15**, 18357 (2013).

[24] O. B. Dor, S. Yochelis, S. P. Mathew, R. Naaman, and Y. Paltiel, A chiral-based magnetic memory device without a permanent magnet, Nat. Commun. **4**, 2256 (2013).

[25] S. P. Mathew, P. C. Mondal, H. Moshe, Y. Mastai, and R. Naaman, Non-magnetic organic/inorganic spin injector at room temperature, Appl. Phys. Lett. **105**, 242408 (2014).

[26] I. Carmeli, K. S. Kumar, O. Heifler, C. Carmeli, and R. Naaman, Spin selectivity in electron transfer in photosystem I, Angew. Chem. Int. Ed. **126**, 9099 (2014).

[27] N. Peer, I. Dujovne, S. Yochelis, and Y. Paltiel, Nanoscale charge separation using chiral molecules, ACS Photon. **2**, 1476 (2015).

[28] P. C. Mondal, N. Kantor-Uriel, S. P. Mathew, F. Tassinari, C. Fontanesi, and R. Naaman, Chiral conductive polymers as spin filters, Adv. Mater. **27**, 1924 (2015).

[29] M. Eckshtain-Levi, E. Capua, S. Refaely-Abramson, S. Sarkar, Y. Gavrilov, S. P. Mathew, Y. Paltiel, Y. Levy, L. Kronik, and R. Naaman, Cold denaturation induces inversion of dipole and spin transfer in chiral peptide monolayers, Nat. Commun. **7**, 10744 (2016).

[30] G. Koplovitz, D. Primc, O. Ben Dor, S. Yochelis, D. Rotem, D. Porath, and Y. Paltiel, Magnetic nanoplatelet-based spin memory device operating at ambient temperatures, Adv. Mater. **29**, 1606748 (2017).

[31] K. Michaeli, V. Varade, R. Naaman, and D. H. Waldeck, A new approach towards spintronics-spintronics with no magnets, J. Phys.: Condens. Matter **29**, 103002 (2017).

[32] V. Varade, T. Z. Markus, K. Vankayala, N. Friedman, M. Sheves, D. H. Waldeck, and R. Naaman, Bacteriorhodopsin based non-magnetic spin filters for biomolecular spintronics, Phys. Chem. Chem. Phys. **20**, 1091 (2018).

[33] J. Banhart, H. Ebert, and A. Vernes, Applicability of the two-current model for systems with strongly spin-dependent disorder, Phys. Rev. B **56**, 10165 (1997).

[34] A. Brataas, Y. V. Nazarov, J. Inoue, and G. E. W. Bauer, Spin accumulation in small ferromagnetic double-barrier junctions, Phys. Rev. B **59**, 93 (1999).

[35] F. J. Jedema, M. S. Nijboer, A. T. Filip, and B. J. van Wees, Spin injection and spin accumulation in all-metal mesoscopic spin valves, Phys. Rev. B **67**, 085319 (2003).

[36] X. Yang, C. H. van der Wal, and B. J. van Wees, Spin-dependent electron transmission model for chiral molecules in mesoscopic devices, Phys. Rev. B **99**, 024418 (2019).

[37] P. Jordan, P. Fromme, H. T. Witt, O. Klukas, W. Saenger, and N. Krauß, Three-dimensional structure of cyanobacterial photosystem I at 2.5 Å resolution, Nature (London) **411**, 909 (2001).

[38] F. J. Jedema, H. B. Heersche, A. T. Filip, J. J. A. Baselmans, and B. J. van Wees, Electrical detection of spin precession in a metallic mesoscopic spin valve, Nature (London) **416**, 713 (2002).

[39] N. F. Mott and H. Jones, *The Theory of the Properties of Metals and Alloys* (Dover, New York, 1958), Chap. VII, pp. 270–271.

[40] A. Fert and I. A. Campbell, Two-Current Conduction in Nickel, Phys. Rev. Lett. **21**, 1190 (1968).

[41] R. Godfrey and M. Johnson, Spin Injection in Mesoscopic Silver Wires: Experimental Test of Resistance Mismatch, Phys. Rev. Lett. **96**, 136601 (2006).

[42] K. Brettel, Electron transfer and arrangement of the redox cofactors in photosystem I, Biochim. Biophys. Acta Bioenergetics **1318**, 322 (1997).

[43] K. Brettel and W. Leibl, Electron transfer in photosystem I, Biochim. Biophys. Acta Bioenergetics **1507**, 100 (2001).

[44] D. Gerster, J. Reichert, H. Bi, J. V. Barth, S. M. Kaniber, A. W. Holleitner, I. Visoly-Fisher, S. Sergani, and I. Carmeli, Photocurrent of a single photosynthetic protein, Nat. Nanotechnol. **7**, 673 (2012).

[45] H. Nakayama, T. Yamamoto, H. An, K. Tsuda, Y. Einaga, and K. Ando, Molecular engineering of rashba spin-charge converter, Sci. Adv. **4**, eaar3899 (2018).

[46] M. Cinchetti, V. A. Dediu, and L. E. Hueso, Activating the molecular spinterface, Nat. Mater. **16**, 507 (2017).

[47] I. Žutić, J. Fabian, and S. Das Sarma, Spintronics: Fundamentals and applications, Rev. Mod. Phys. **76**, 323 (2004).

[48] K. Takanashi, Fundamentals of magnetoresistance effects, in *Spintronics for Next Generation Innovative Devices* (Wiley, Chichester, UK, 2015).

[49] P. M. Tedrow and R. Meservey, Spin-Dependent Tunneling Into Ferromagnetic Nickel, Phys. Rev. Lett. **26**, 192 (1971).

[50] J. S. Moodera, L. R. Kinder, T. M. Wong, and R. Meservey, Large Magnetoresistance at Room Temperature in Ferromagnetic Thin Film Tunnel Junctions, Phys. Rev. Lett. **74**, 3273 (1995).

[51] Yu. Lu, X. W. Li, G. Xiao, R. A. Altman, W. J. Gallagher, A. Marley, K. Roche, and S. Parkin, Bias voltage and temperature dependence of magnetotunneling effect, J. Appl. Phys. **83**, 6515 (1998).

[52] J. Bass and W. P. Pratt, Jr., Spin-diffusion lengths in metals and alloys, and spin-flipping at metal/metal interfaces: an experimentalist's critical review, J. Phys.: Condens. Matter **19**, 183201 (2007).

[53] M. H. D. Guimarães, P. J. Zomer, J. Ingla-Aynés, J. C. Brant, N. Tombros, and B. J. van Wees, Controlling Spin Relaxation in Hexagonal BN-Encapsulated Graphene with a Transverse Electric Field, Phys. Rev. Lett. **113**, 086602 (2014).

[54] J. Ingla-Aynés, M. H. D. Guimarães, R. J. Meijerink, P. J. Zomer, and B. J. van Wees, 24-μm spin relaxation length in boron nitride encapsulated bilayer graphene, Phys. Rev. B **92**, 201410(R) (2015).

[55] N. Tombros, C. Jozsa, M. Popinciuc, H. T. Jonkman, and B. J. van Wees, Electronic spin transport and spin precession in single graphene layers at room temperature, Nature (London) **448**, 571 (2007).

[56] C. N. Berglund and W. E. Spicer, Photoemission studies of copper and silver: Theory, Phys. Rev. **136**, A1030 (1964).

[57] C. N. Berglund and W. E. Spicer, Photoemission studies of copper and silver: Experiment, Phys. Rev. **136**, A1044 (1964).

[58] W. Kuch and C. M. Schneider, Magnetic dichroism in valence band photoemission, Rep. Prog. Phys. **64**, 147 (2001).